


# High-resolution detection of surface potential in strained $MoS_2$ by multifrequency electrostatic force microscopy

Ya-Nan Chen(陈亚楠), Jian-Qiang Qian(钱建强), Ying-Zi Li(李英姿), Hao-Wei Sun(孙浩崴), Rui Lin(林锐), Peng Cheng(程鹏), Ming-Hao Wang(王铭浩), Yong-Chang Li(李永畅), and Yi-Zhe Yu(俞伊哲)
**Citation:**Chin. Phys. B, 2026, 35 (**8**): 080704. DOI: 10.1088/1674-1056/ae445d
http://cpb.iphy.ac.cn; http://iopscience.iop.org/cpb

**What follows is a list of articles you may be interested in**

---

## Memristive neural network circuit with fault tolerance for character recognition

Mei Guo(郭梅), Jikang Liu(刘继康), and Jingzhi Xu(徐景芝)
Chin. Phys. B, 2026, 35 (**6**): 060702. DOI: 10.1088/1674-1056/ae3f94

## Echolocation-inspired memristive behavioral decision circuit

Yueqi Song(宋钥淇), Xiaozhou He(何晓舟), Xianying Xu(徐宪莹), Yinghong Cao(曹颖鸿), Santo Banerjee, Suo Gao(高锁), and Jun Mou(牟俊)
Chin. Phys. B, 2026, 35 (**6**): 060701. DOI: 10.1088/1674-1056/ae2d3e

## Multiparameter hierarchical sensitivity analysis of tilt-to-length coupling noise in Taiji science interferometer

Fei Xie(谢菲), Xiaodong Peng(彭晓东), Wenlin Tang(唐文林), Mengyuan Zhao(赵梦圆), and Xiaoshan Ma(马晓珊)
Chin. Phys. B, 2026, 35 (**1**): 010701. DOI: 10.1088/1674-1056/ae07a8

## Testing algorithm for the computation of the transverse emittance of the ion beams generated by the ECR mVINIS ion source based on a pepper-pot method

Viktor Jocić, Igor Telečki, and Ivan Trajić
Chin. Phys. B, 2025, 34 (**6**): 060701. DOI: 10.1088/1674-1056/adc674

## Text-guided diverse-expression diffusion model for molecule generation

Wenchao Weng(翁文超), Hanyu Jiang(蒋涵羽), Xiangjie Kong(孔祥杰), and Giovanni Pau
Chin. Phys. B, 2025, 34 (**5**): 050701. DOI: 10.1088/1674-1056/adbedd

---

# High-resolution detection of surface potential in strained $MoS_2$ by multifrequency electrostatic force microscopy

Ya-Nan Chen(陈亚楠), Jian-Qiang Qian(钱建强)†, Ying-Zi Li(李英姿), Hao-Wei Sun(孙浩崴), Rui Lin(林锐), Peng Cheng(程鹏), Ming-Hao Wang(王铭浩), Yong-Chang Li(李永畅), and Yi-Zhe Yu(俞伊哲)

*School of Physics, Beihang University, Beijing* 100191, *China*

(Received 13 November 2025; revised manuscript received 3 February 2026; accepted manuscript online 11 February 2026)

Detection and mechanistic investigation of out-of-plane surface potential variations induced by strain gradients in two-dimensional materials remain a bottleneck for understanding local electromechanical coupling at the nanoscale. Here, we develop a quantitative multifrequency electrostatic force microscopy (MF-EFM) method which, by establishing a quantitative relationship between the response of the probe in the second mode and the sample surface potential, enables precise measurement of the electrical properties in wrinkled regions of $MoS_2$ films. We find that the potential distribution in these regions is consistent with estimates based on the flexoelectric effect induced by strain gradients, both being on the order of a few millivolts. This study directly demonstrates the modulation of local electronic properties in transition metal dichalcogenides by strain gradients and confirms the potential of MF-EFM, owing to its superior spatial resolution, for electrical characterization of advanced materials.

**Keywords:** electrostatic force microscopy, multifrequency, $MoS_2$, electric potential, high resolution

**PACS:** 07.79.Lh, 68.37.–d, 77.65.–j

**DOI:** 10.1088/1674-1056/ae445d **CSTR:** 32038.14.CPB.ae445d

## 1. Introduction

Two-dimensional (2D) semiconductors, such as h-BN,[1] transition metal dichalcogenides (TMDs),[2–4] hold the potential to overcome the inherent limitations of conventional semiconductors such as drain-induced barrier lowering, mobility degradation caused by interface scattering, and the restricted current on/off ratio determined by the semiconductor bandgap. These unique advantages have sparked extensive research in this field.[5–7] 2D materials have superior electronic properties[8–13] and mechanically flexible nature.[14–16] Molybdenum disulfide ($MoS_2$) is the most common wide-bandgap semiconductor material. Wu *et al.* first observed piezoelectricity of monolayer $MoS_2$, revealing that only intrinsic in-plane piezoelectricity exists in these 2D materials and the piezoelectric effect is confined in odd-layers of TMDs.[17] Mao *et al.* transferred bilayer $MoS_2$ onto a nanocone-patterned substrate and observed the emergence of unexpected vertical ferroelectricity in $MoS_2$.[18] Jie Jiang's team reported an experimental demonstration of the flexo-photovoltaic effect in $MoS_2$ by using a strain-gradient engineering approach, unveiling the fundamental relation between the flexo-photovoltaic effect and a strain gradient in low-dimensional materials.[19] Sabir Hussain *et al.* investigated strain-induced hierarchical ripple nanostructures in triangular $MoS_2$ flakes, proving that the mechanical, electronic, and optical spectra characteristics of $MoS_2$ were significantly modified due to the suffering from large tensile strain.[20]

The practical implementation of 2D materials critically depends on their electrical characteristics. Nanoscale characterization of these properties is therefore imperative. However, the aforementioned studies focused on measuring the nanoscale piezoelectric and resistive switching behaviors of 2D materials using piezoresponse force microscopy (PFM) and conductive atomic force microscopy (C-AFM), while overlooking the characterization of the surface potential of the samples. KPFM is a commonly used technique for characterizing the surface potential of a sample. However, because it relies on working through a DC bias closed-loop feedback, the applied external electric field may interfere with the sample's original charge state, making it difficult to obtain the true intrinsic electrical properties.[21] Electrostatic force microscopy (EFM), which evolved from atomic force microscopy (AFM), emerges as a powerful scanning probe technique capable of detecting localized potential variations with nanoscale spatial resolution and provides a vast and valuable contribution to understanding and engineering increasingly complex nanoscale materials and devices.[22–25] By monitoring phase/amplitude changes in long-range electrostatic forces between the probe and sample surface, EFM enables analysis of charge injection, transport, trapping, and interfacial electrical double-layer evolution. This technique holds significant promise for investigating edge-state effects, defect-mediated charge trapping, and surface potential inhomogeneity in 2D material systems.[26–29]

Conventional lift mode EFM operates based on a two-pass scanning principle. In the first scan, the sample's topog-

†Corresponding author. E-mail: qianjq@buaa.edu.cn

© 2026 Chinese Physical Society and IOP Publishing Ltd. All rights, including for text and data mining, AI training, and similar technologies, are reserved.

raphy is measured. Subsequently, the probe is raised to a certain height along the first scan, and a DC bias is applied to the probe during the second pass to acquire the sample's surface electrical information.[30,31] To achieve higher resolution and enhanced sensitivity, AFM imaging has been increasingly explored using higher harmonic detection, alternative flexural and torsional cantilever modes.[31,32] Stark *et al.* achieved parallel characterization of surface topography and charge patterns by operating AFM in amplitude modulation mode while applying a modulated bias voltage to excite a higher flexural eigenmode, known as multifrequency electrostatic force microscopy (MF-EFM).[33,34] Jose R. Lozano and Ricardo Garcia developed a theory for multifrequency AFM, demonstrating enhanced sensitivity and material contrast through bimodal excitation.[35,36]

In this work, we derived the relationship between the second mode amplitude of the MF-EFM mode and the surface potential of the sample, enabling the quantitative measurement of the sample surface potential using an open-loop method. This method successfully detected the weak potential fluctuations induced by the strain gradient in $MoS_2$, with the measured values aligning with theoretical estimates based on flexoelectricity. This work experimentally links strain gradients to local potential variations in TMDs, providing a solid experimental foundation for understanding and ultimately utilizing strain engineering to tune the electronic properties of two-dimensional materials. Compared to conventional lift mode EFM, MF-EFM effectively reduces topographic crosstalk while simultaneously enhancing the resolution of both topographic and electrostatic force signals. By using probes with higher resonance frequencies, we further achieved superior resolution, highlighting the significant potential of this technique in the characterization of low-dimensional materials.

## 2. Results and discussion

The working principle of MF-EFM involves simultaneously exciting or detecting multiple frequencies. Figure 1 illustrates the schematic diagram of the MF-EFM system, which consists of a commercial AFM (XE-100, Park Systems) and a lock-in amplifier (Zurich Instruments HF2LI). Lock-in 1 and Lock-in 2 denote the internal lock-in amplifier of the AFM and the external lock-in amplifier, respectively. The AFM operates in amplitude modulation mode, where the built-in lock-in amplifier (Lock-in 1) excites the piezoelectric actuator to drive the cantilever at its first flexural resonance mode for topographic imaging. Meanwhile, the external lock-in amplifier (Lock-in 2) outputs a sinusoidal AC voltage applied to the conductive probe to excite electrostatic interactions near the second flexural resonance mode for electrical imaging. In MF-EFM, different flexural resonance modes of the AFM cantilever are employed to separately detect topographic and electrostatic information. The first flexural resonance mode ($f_1$) is used for conventional amplitude-modulation imaging to obtain surface topography, while the second flexural resonance mode ($f_2$) is selectively excited by the applied AC voltage to enhance sensitivity to electrostatic forces. By detecting the cantilever response at $f_2$, MF-EFM effectively decouples electrostatic signals from topographic interactions, thereby suppressing topographic crosstalk and enabling high-resolution detection of weak surface potential variations. The electrostatic force between the tip and the sample is

$$F_{\mathrm{e}}(t) = \frac{1}{2}\frac{\mathrm{d}C}{\mathrm{d}D}\left[U_{\mathrm{s}} - U_{\mathrm{AC}}\sin(\omega t)\right]^2, \tag{1}$$

where $\mathrm{d}C/\mathrm{d}D$ is the capacitance gradient between the tip and the sample, $U_{\mathrm{s}}$ is the surface potential of the sample, and $U_{\mathrm{AC}}\sin(\omega t)$ is the AC modulation excitation. The equation of motion of the cantilever under the action of electrostatic force and mechanical excitation is

$$\frac{\ddot{z}_i}{\omega_i^2} + \frac{\dot{z}_i}{\omega_i Q_i} + z_i = \frac{F_{\mathrm{e}i}(t)}{k_i} + \frac{F_{\mathrm{m}i}(t)}{k_i}, \tag{2}$$

where $i$ represents the mode order of the cantilever, $F_{\mathrm{e}i}$ is the electrostatic force component of the $i$-th mode, $F_{\mathrm{m}i}$ is the mechanical force component of the $i$-th mode, and $z_i$, $\omega_i$, $Q_i$, and $k_i$ are the amplitude, frequency, quality factor, and stiffness of the cantilever's $i$-th mode, respectively. By deriving Eq. (2), the amplitude of the second mode of the probe during stable vibration can be obtained as

$$A(\omega_2) = \frac{2\pi\varepsilon_0 Q_2}{k_2}\cdot\frac{1}{\left(\frac{z_a}{R}\right)^2 + \frac{z_a}{R}}U_{\mathrm{s}}U_{\mathrm{AC}}. \tag{3}$$

Here, $R$ is the probe radius, and $z_a$ is the initial probe lift height. Equation (3) indicates that the electrostatic amplitude is proportional to the surface potential of the sample. As shown in supplementary Fig. S1, the experiment verified the derived amplitude–voltage relationship. Under low excitation voltage, the amplitude and phase of the probe are nearly proportional. And the probe is calibrated based on this relationship. The fitted curve obtained from Fig. S1 is

$$A_{\mathrm{e}} = 683.3U_{\mathrm{s}} - 16.85, \tag{4}$$

where $A_{\mathrm{e}}$ is the electrostatic amplitude demodulated by the lock-in amplifier at the second-mode frequency. When measuring the standard sample, the probe signal was attenuated by a factor of 20 before being fed into the lock-in amplifier. After demodulation by the lock-in amplifier, the signal was amplified 400× and sent to the auxiliary input of the AFM for imaging. When characterizing 2D material samples, because the signal was weaker, the 20× attenuator was not used. Instead, the signal was fed directly into the lock-in amplifier for demodulation. After demodulation, the signal was amplified

100× and sent to the AFM auxiliary input for imaging. Therefore, the amplitude–potential relationship is

$$A_e = 3416.5U_s - 84.25. \quad (5)$$

All subsequent electrostatic amplitude images have been converted into the measured sample surface potential.

The $MoS_2$ films grown on the $SiO_2$/Si substrate are selected to demonstrate the high spatial resolution characterization capability of MF-EFM. Detailed growth conditions can be found in Fig. S2.

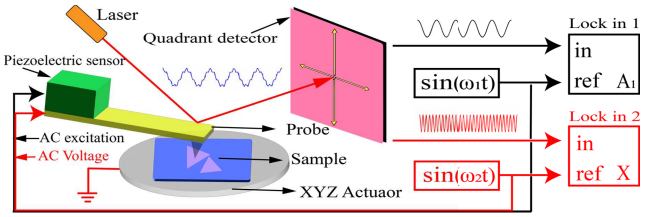



**Fig. 1.** Scheme of the MF-EFM.

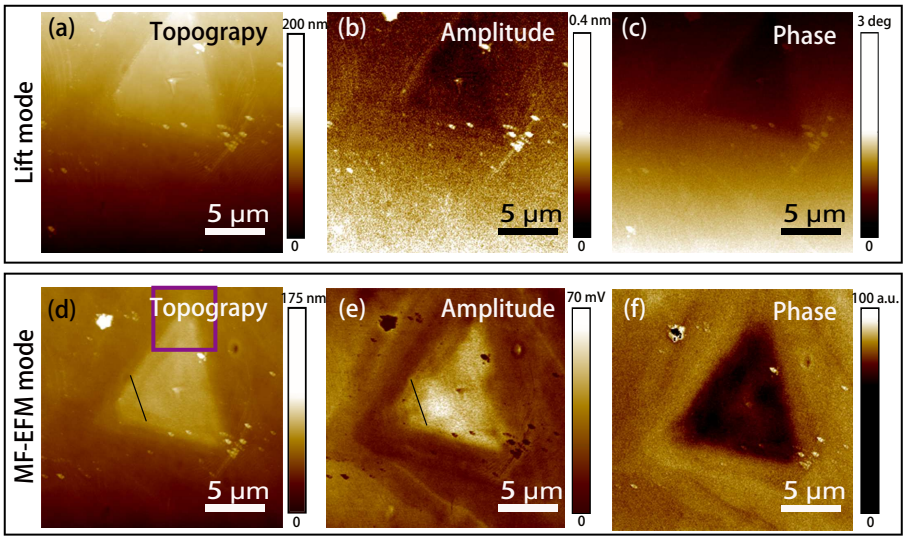



**Fig. 2.** (a)–(c) Topographic, EFM amplitude and phase images of $MoS_2$ obtained by lift mode EFM. (d)–(f) Topographic, EFM amplitude and phase images of $MoS_2$ obtained by MF-EFM. All measurements were performed using a cantilever with flexural resonances $f_1 = 71.4$ kHz and $f_2 = 457.5$ kHz. The scan area is 20 μm × 20 μm.

The first-order ($f_1$) and second-order ($f_2$) free resonance frequencies of the probe cantilever in air are approximately 71.4 kHz and 457.5 kHz, respectively. The topography, electrostatic amplitude, and phase images of a multilayer-stacked $MoS_2$ sample obtained using the conventional lift mode EFM where the tip–sample distance is about 30 nm, and the tip bias are 3 V are shown in Figs. 2(a)–2(c). The corresponding MF-EFM images acquired over the same area are shown in Figs. 2(d)–2(f), with an AC voltage ($V_{ac}$) of 1 V at 457.5 kHz applied between the conductive tip and the sample during scanning. Compared with the conventional lift mode method, imaging by the MF-EFM method preserves mostly consistent physical characteristics, but superior details and sharper edges. As shown in Fig. 2(a), the sample exhibits a certain degree of tilt along the slow scan direction. Although the conventional lift mode EFM claims to eliminate the influence of van der Waals forces by recording the topography during the first scan and lifting the probe along the recorded curves during the second scan, this approach imposes high demands on the scanning control system. Figures 2(b) and 2(c) clearly illustrate that the electrostatic amplitude and phase are affected by the topographical tilt, and that significant tilt can obscure subtle electrical variations on the sample surface. In conventional EFM mode, it is difficult to eliminate the influence of topography, whereas the electrical signals in MF-EFM mode are almost unaffected by topography. No tilting similar to that observed in the topography is present in the amplitude and phase images, as shown in Figs. 2(e) and 2(f). The region within the purple square in Fig. 2(d) is selected for testing, and the results are shown in Fig. 3. A closer examination of the zoomed-in images reveals distinct striped wrinkles in Figs. 3(a) and 3(d). Meanwhile, the corresponding electrostatic signals measured using the MF-EFM mode in Figs. 3(e) and 3(f) show clear amplitude variations. However, no such electrical signals are observed in the regions shown in Figs. 3(b) and 3(c), measured using lift mode EFM. Figures 3(e) and 3(f) show the data curves at the white lines in the topography and EFM amplitude images for lift mode and MF-EFM modes, respectively.

From the data, it is evident that the wrinkle height ranges from 1 nm to 4 nm, with a half-width between 100 nm and 200 nm. The topography and electrostatic amplitude images in the MF-EFM mode are closely related but exhibit opposite trends. In contrast, the lift mode did not detect any potential fluctuations. This phenomenon suggests that the weak potential fluctuations detected by MF-EFM may originate from the flexoelectric field generated by the bending of $MoS_2$. The in-

version symmetry can be broken by a strain gradient[19]

$$\eta_{lmn} = \frac{\partial u_{mn}}{\partial x_l}. \tag{6}$$

Here, $u_{mn}$ is the strain tensor, and $x_l$ is the spatial coordinate. In the absence of an external electric field, the polarization $P_i$ induced by the strain gradient $\eta_{lmn}$ corresponds to the flexoelectric effect, which is governed by the flexoelectric coefficient

$$\mu_{ilmn} = \frac{\partial P_i}{\partial \eta_{lmn}}. \tag{7}$$

Here, $\mu_{ilmn}$ is a fourth-order tensor, and the flexoelectric effect is symmetrically allowed in any material. We assume that the wrinkle stripe has a height of 4 nm and a half-width of 190 nm, and the shape of the wrinkle is parabolic: $z(x) = \frac{1}{2}\kappa x^2$. According to formula (6), the strain gradient $\eta_{lmn}$ at the vertex is $2.22 \times 10^{-4}$ nm$^{-1}$. Assuming the out-of-plane flexoelectric coefficient $\mu_{ilmn}$ of $MoS_2$ is 0.4758 nC/m,[37] according to formula (7), the polarization $P_i$ is approximately $1.06 \times 10^{-4}$ C/m$^2$. We used a simplified capacitor-like model to estimate the flexoelectric-induced potential, which does not account for full dielectric screening effects. The potential difference is estimated using the following expression:

$$\Delta V = \frac{P_i d}{\varepsilon_0 \varepsilon_r}. \tag{8}$$

Here, $d$ is an effective screening (charge-separation) length that characterizes the out-of-plane separation between flexoelectrically induced bound charges, $\varepsilon_0$ is the vacuum permittivity, and $\varepsilon_r$ is the relative dielectric constant of the medium between the sample surface and the AFM tip. In this estimation, $\varepsilon_r = 1$ is adopted to approximate the air environment, thus providing an upper-bound estimate without full dielectric screening. For monolayer $MoS_2$, $d$ is taken as 0.32 nm, corresponding to the intrinsic thickness of a single S–Mo–S trilayer.[38] Using $\varepsilon_0 = 8.85 \times 1^{-12}$ F/m, the estimated surface potential is approximately 3.83 mV.

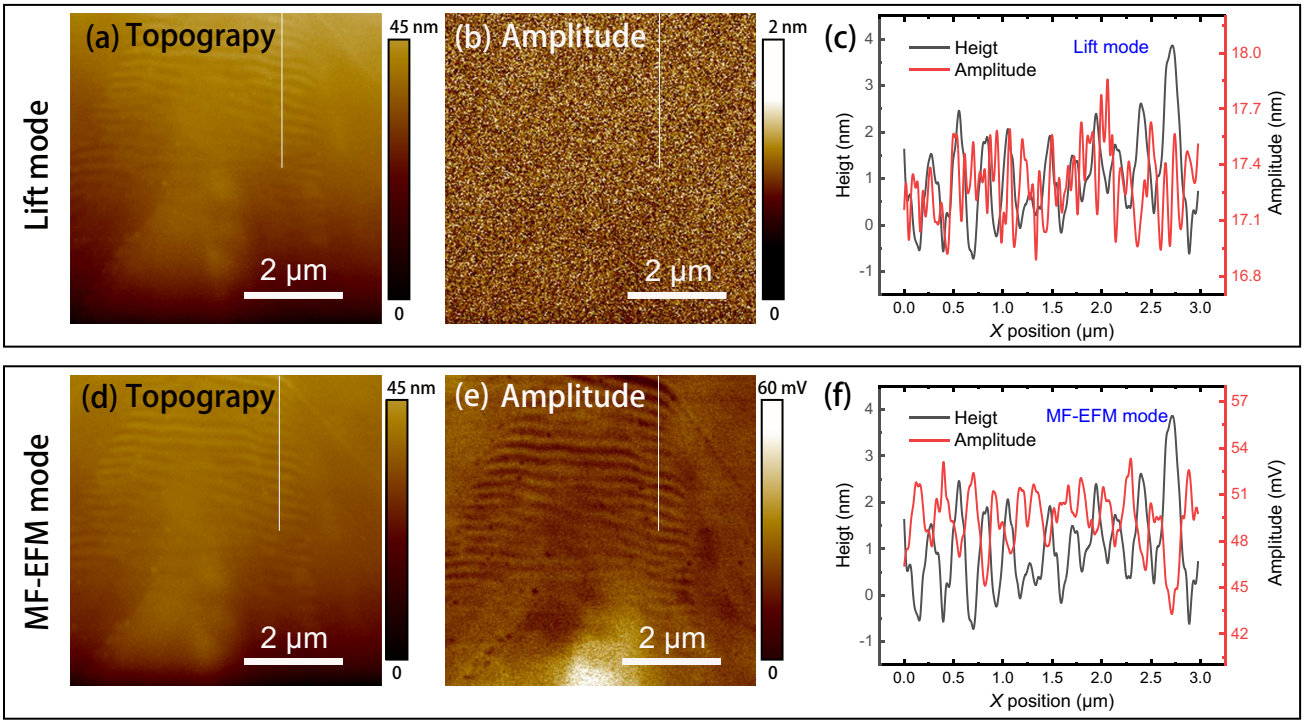



**Fig. 3.** (a)–(c) Topography, lift mode EFM electrostatic amplitude image, and the corresponding line profiles extracted along the white lines for wrinkled $MoS_2$. (d)–(f) Corresponding topography, MF-EFM electrostatic amplitude image, and line profiles acquired from the same region. All measurements were performed with a cantilever operated at the first and second flexural resonance modes, $f_1 = 71.4$ kHz and $f_2 = 457.5$ kHz. The scanned area corresponds to the 6 μm × 6 μm purple square marked in Fig. 2(d).

We established the relationship between electrostatic amplitude and surface potential, converting the measured amplitude into the surface potential of the sample. As shown in Fig. 3(f), the measured surface potential fluctuations are within the ∼ 10 mV range. In contrast, MF-EFM measurements performed in flat, wrinkle-free regions exhibit negligible surface potential contrast (see supplementary Fig. S3), indicating that the observed potential variations are strongly correlated with local strain gradients rather than extrinsic effects such as surface contamination or contact potential differences. The experimentally observed surface potential fluctuations are of the same order of magnitude as the estimated flexoelectric-induced potential (∼ 3.83 mV) obtained from the simplified model. The remaining discrepancy may arise from variations in wrinkle geometry, local dielectric screening, and tip–sample coupling. Similar strain-gradient-induced flexoelectric polarization in monolayer $MoS_2$ has been theoretically reported, where the induced polarization is shown to

scale with local strain gradients rather than uniform strain or piezoelectric contributions.[39] These results support the attribution of the observed surface potential variations in $MoS_2$ thin films primarily to strain-gradient-induced flexoelectric effects. MF-EFM thus demonstrates its capability for investigating the physical mechanisms by which strain gradients regulate local electronic properties in transition metal dichalcogenides.

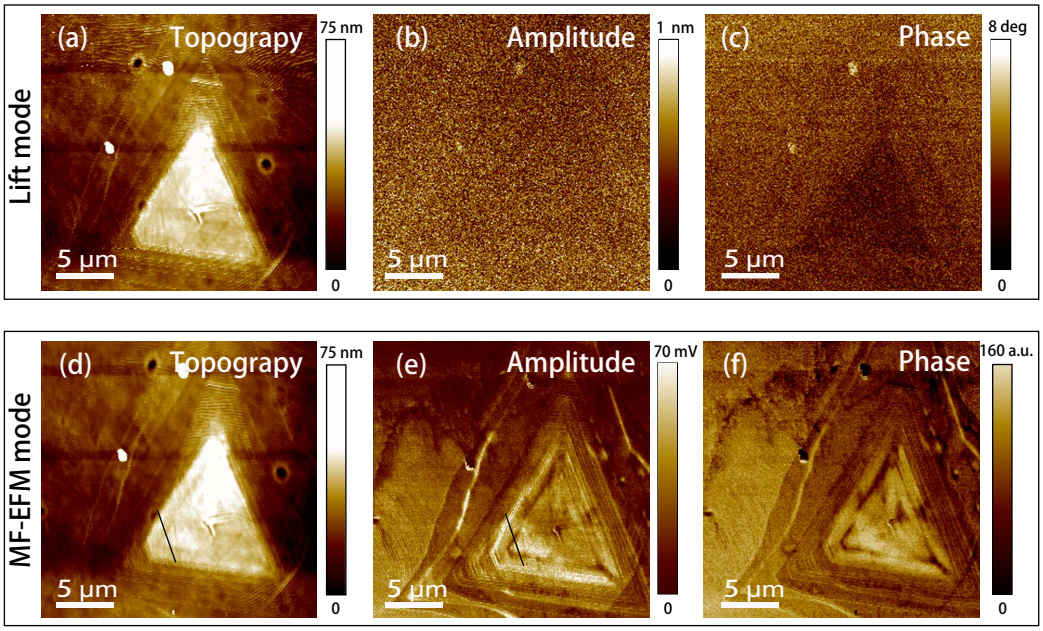



**Fig. 4.** (a)–(c) Topography, lift mode EFM electrostatic amplitude, and phase images of wrinkled $MoS_2$. (d)–(f) Corresponding topography, MF-EFM electrostatic amplitude, and phase images acquired from the same region. All measurements were performed with a cantilever operated at the first and second flexural resonance modes, $f_1 = 108.3$ kHz and $f_2 = 682.8$ kHz. The scan area is 20 μm × 20 μm.

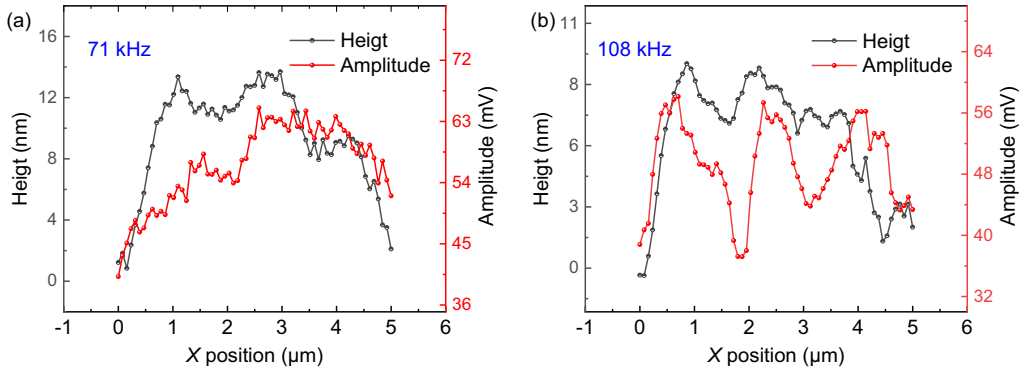



**Fig. 5.** Topography and electrostatic amplitude profiles taken at nearly identical positions along the black lines in Figs. 2 and 4. (a) 71 kHz and (b) 108 kHz.

To further improve the resolution, we used a probe with a higher frequency to test the $MoS_2$ film. The cantilever with the flexural resonances $f_1 = 108.3$ kHz, $f_2 = 682.8$ kHz is employed. Both lift mode EFM and MF-EFM were performed at the same location, and the results are shown in Fig. 4. Figures 4(a)–4(c) present the topographic, electrostatic amplitude, and phase images obtained via conventional EFM, while Figs. 4(d)–4(f) display corresponding results from MF-EFM. All images undergo first-order flattening processing to eliminate vertical tilt artifacts. Compared with the 71 kHz probe, both EFM and MF-EFM modes deliver sharper topographic images, resolving stripe-like wrinkles around triangular multilayer structures without requiring enlarged scans, as shown in Figs. 4(a) and 4(d). Interestingly, in Figs. 4(b)–4(c), the conventional lift mode EFM exhibits degraded electrostatic signals compared to test results with lower flexural resonance cantilevers. The EFM amplitude images display minimal potential fluctuations, with only a subtle contrast observed in the phase. In stark contrast, MF-EFM achieved exceptional resolution. This phenomenon can be explained by the fact that although higher test frequencies intrinsically improve spatial resolution, the higher spring constant (increased stiffness) of probes in conventional lift mode EFM diminishes their sensitivity to weak electrostatic forces. Conversely, MF-EFM eliminates the lift mode constraint, allowing stronger electrostatic interactions to effectively probe surface potentials

while retaining high-frequency advantages. These observations demonstrate that conventional EFM suffers from fundamental limitations in reconciling resolution enhancement with force sensitivity, whereas MF-EFM circumvents this trade-off. The ability of MF-EFM to leverage high-frequency probes for resolution improvement holds particular significance for semiconductor characterization.

We extracted the data curves from the black lines at nearly identical positions in the topography and electrostatic amplitude measured under the MF-EFM mode in Figs. 2 and 4. The results are presented in Fig. 5. At the same scan speed, the high-frequency probe vibrates more stably, resulting in smoother topography curves, while the electrostatic curves have higher resolution, demonstrating a strong ability to characterize local electric potential.

## 3. Conclusion

Starting from the equation of motion of the probe, we derived the relationship between the probe's second mode and the surface potential of the sample, converting the electrostatic amplitude into the measured surface potential. Using this method, we quantitatively studied the electrical characteristics of the wrinkle region on the $MoS_2$ surface. The measured potential distribution is of the same order of magnitude, revealing the physical mechanism of strain gradient regulation of local electronic properties in transition metal dichalcogenides. By using a higher-frequency probe, we further improved the resolution of potential measurements, demonstrating the potential of quantitative MF-EFM in characterizing local electronic properties of advanced materials.

## Acknowledgment

Project supported by the National Natural Science Foundation of China (Grant Nos. 62171012 and 62271032).

## References

[1] Yasuda K, Wang X R, Watanabe K, Taniguchi T and Jarillo-Herrero P 2021 *Science* **372** 1458
[2] Zeng S F, Liu C S and Zhou P 2024 *Nat. Rev. Electr. Eng.* **1** 335
[3] Ao M R, Zhou X C, Kong X J, Gou S F, Chen S F, Dong X Q, Zhu Y X, Sun Q C, Zhang Z J, Zhang J S, Zhang Q R, Hu Y, Sheng C M, Wang K X, Wang S Y, Wan J, Han J, Bao W Z and Zhou P 2025 *Nature* **640** 654
[4] Liang B X, Liu L H, Tang J C, Chen J, Shi Y and Li S L 2023 *Chin. Phys. Lett.* **40** 058503
[5] Geim A K and Grigorieva I V 2013 *Nature* **499** 419
[6] Li T T, Guo W, Ma L, Li W S, Yu Z H, Han Z, Gao S, Liu L, Fan D X, Wang Z X, Yang Y, Lin W Y, Luo Z Z, Chen X Q, Dai N X, Tu X C, Pan D F, Yao Y G, Wang P, Nie Y F, Wang J L, Shi Y and Wang X R 2021 *Nat. Nanotechnol.* **16** 1201
[7] Wu K, Wang H, Yang M, Liu L, Sun Z Y, Hu G J, Song Y P, Han X, Guo J G, Wu K H, Feng B J, Shen C M, Huang Y, Shi Y G, Cheng Z G, Yang H T, Bao L H, Pantelides S T and Gao H J 2024 *Adv. Mater.* **36** 2313511
[8] Zhang N, Surrente A, Baranowski M, Maude D K, Gant P, Castellanos-Gomez A and Plochocka P 2018 *Nano Lett.* **18** 7651
[9] Tran K, Moody G, Wu F C, Lu X B, Choi J, Kim K, Rai A, Sanchez D A, Quan J M, Singh A, Embley J, Zepeda A, Campbell M, Autry T, Taniguchi T, Watanabe K, Lu N S, Banerjee S K, Silverman K L, Kim S, Tutuc E, Yang L, MacDonald A H and Li X Q 2019 *Nature* **567** 71
[10] Xia Q, Hu Y, Wang Y P, Zhang C W, Ren M J, Li S S and Ji W X 2022 *Nanoscale* **14** 1264
[11] Varghese A, Pandey A H, Sharma P, Yin Y F, Medhekar N V and Lodha S 2024 *Nano Lett.* **24** 8472
[12] Xia Q, Li N, Ji W X, Zhang C W, Ding M, Ren M J and Li S S 2023 *Nanoscale* **15** 1365
[13] Wu F F, Li L, Xu Q L, Liu L, Yuan Y L, Zhao J J, Huang Z H, Zan X Z, Watanabe K, Taniguchi T, Shi D X, Xian L D, Yang W, Du L J and Zhang G Y 2023 *Chin. Phys. Lett.* **40** 047303
[14] Daus A, Vaziri S, Chen V, Köroğlu Ç, Grady R W, Bailey C S, Lee H R, Schauble K, Brenner K and Pop E 2021 *Nat. Electron.* **4** 495
[15] Wang J W, He L Q, Zhang Y H, Nong H Y, Li S N, Wu Q K, Tan J Y and Liu B L 2024 *Adv. Mater.* **36** 2314145
[16] Hsu C C, Teague M L, Wang J Q and Yeh N C 2020 *Sci. Adv.* **6** eaat9488
[17] Wu W Z, Wang L, Li Y L, Zhang F, Lin L, Niu S M, Chenet D, Zhang X, Hao Y F, Heinz T F, Hone J and Wang Z L 2014 *Nature* **514** 470
[18] Mao J F, He J Y, Io W F, Guo F, Wu Z, Yang M and Hao J H 2024 *ACS Nano* **18** 30360
[19] Jiang J, Chen Z Z, Hu Y, Xiang Y, Zhang L F, Wang Y P, Wang G C and Shi J 2021 *Nat. Nanotechnol.* **16** 894
[20] Hussain S, Xu R, Xu K Q, Lei L, Meng L, Zheng Z Y, Xing S Y, Guo J F, Dong H Y, Liaqat A, Iqbal M A, Li Y J, Sugawara Y, Pang F, Ji W, Xie L M and Cheng Z H 2020 *Appl. Phys. Lett.* **117** 153102
[21] Xu J and Chen D Y 2021 *J. Appl. Phys.* **129** 034301
[22] Girard P 2001 *Nanotechnology* **12** 485
[23] Lucchesi M, Privitera G, Labardi M, Prevosto D, Capaccioli S and Pingue P 2009 *J. Appl. Phys.* **105** 054301
[24] Datta S S, Strachan D R, Mele E J and Johnson A T C 2009 *Nano Lett.* **9** 7
[25] Xu K Q, Xie Y F, Ma S Q, Liang Q and Shi Z W 2024 *ACS Appl. Mater. Interfaces* **16** 39867
[26] Coffey D C and Ginger D S 2006 *Nat. Mater.* **5** 735
[27] Collins L, Kilpatrick J I, Kalinin S V and Rodriguez B J 2018 *Rep. Prog. Phys.* **81** 086101
[28] Fumagalli L, Gramse G, Esteban-Ferrer D, Edwards M A and Gomila G 2010 *Appl. Phys. Lett.* **96** 183107
[29] Gramse G, Kölker A, Škereň T, Stock T J Z, Aeppli G, Kienberger F, Fuhrer A and Curson N J 2020 *Nat. Electron.* **3** 531
[30] Hussain S, Xu K Q, Ye S L, Lei L, Liu X M, Xu R, Xie L M and Cheng Z H 2019 *Front. Phys.* **14** 33401
[31] Avila A and Bhushan B 2010 *Crit. Rev. Solid State Mater. Sci.* **35** 38
[32] Gisbert V G and Garcia R 2021 *ACS Nano* **15** 20574
[33] Stark R W, Naujoks N and Stemmer A 2007 *Nanotechnology* **18** 065502
[34] Ding X D, An J, Xu J B, Li C and Zeng R Y 2009 *Appl. Phys. Lett.* **94** 223109
[35] Lozano J R and Garcia R 2008 *Phys. Rev. Lett.* **100** 076102
[36] Lozano J R and Garcia R 2009 *Phys. Rev. B* **79** 014110
[37] Sun L, Javvaji B, Zhang C L, Zhuang X Y and Chen W Q 2022 *Nano Energy* **102** 107701
[38] Ahuja U, Dashora A, Tiwari H, Kothari D C and Venugopalan K 2014 *Comput. Mater. Sci.* **92** 451
[39] Yang Y D, Hirsinger L and Devel M 2022 *J. Chem. Phys.* **156** 174104